Development of time-varying global gridded Ts-Tm model for precise GPS-PWV retrieval

Peng Jiang[1, 2], Shirong Ye[2], Yinhao Lu[1], Yanyan Liu[3, 2], Dezhong Chen[2], Yanlan Wu[1]
[1]School of Resources and Environmental Engineering, Anhui University, Hefei, Anhui, China,
[2]GNSS Research Center, Wuhan University, Wuhan, Hubei, China,
[3]Shenzhen Key Laboratory of Spatial Smart Sensing and Services, College of Civil Engineering, Shenzhen University, Shenzhen, Guangdong, China

Correspondence to: Peng Jiang (jiangpeng@ahu.edu.cn)

Abstract: Water-vapor-weighted mean temperature, T_m, is the key variable for estimating the mapping factor between GPS zenith wet delay (ZWD) and precipitable water vapor (PWV). For the near real-time GPS-PWV retrieving, estimating T_m from surface air temperature T_s is a widely used method because of its high temporal resolution and a fair degree of accuracy. Based on the estimations of T_m and T_s at each reanalysis grid node of the ERA-Interim data, we analyzed the relationship between T_m and T_s without data smoothing. The analyses demonstrate that the T_s–T_m relationship has significant spatial and temporal variations. Static and time-varying global gridded T_s–T_m models were established and evaluated by comparisons with the radiosonde data at 723 radiosonde stations in the Integrated Global Radiosonde Archive (IGRA). Results show that our global gridded T_s–T_m equations have prominent advantages over the other globally applied models. At a considerable number of stations, the gridded T_s–T_m models can remove the large biases in Bevis equation and in the latitude-related linear model. Multiple statistical tests at the 5 % significance levels show that the time-varying global gridded model is superior to the other models at 60.03 % of the radiosonde sites. The second-best model is the 1° × 1° GPT2w model, which is superior at only 12.86 % of the sites. The contribution of the T_m's uncertainty to the total uncertainty of GPS PWV also dropped significantly. GPS-PWV retrievals using different T_m estimates were compared at 74 IGS stations. At most of the sites, the relative differences of GPS-PWV are within 1 % by applying time-varying global gridded T_s–T_m equations. This performance is superior to the other T_m estimation models. The differences between GPS-PWV and radiosonde PWV are influenced by multiple factors instead of a single T_m parameter. However, evident improvements still exist at particular sites by using more precise T_s–T_m equations. PWV errors could decrease 1~2 mm during the wetter months.

1. Introduction

Water vapor is an important trace gas and one of the most variable components in the troposphere. The transport, concentration, and phase transition of water vapor are directly involved in the atmospheric radiation and hydrological cycle. It plays a key role in many climate changes and weather processes (Adler et al., 2016; Mahoney et al., 2016; Song et al., 2016). However, water vapor has high spatial-temporal variability, and its content is often small within the atmosphere. It is a challenge to measure water vapor content accurately and timely. For decades, several methods have been studied, such as radiosondes and water vapor radiometers, sun photometers, and GPS (Campmany et al., 2010; Ciesielski et al., 2010; Liu et al., 2013; Perez-Ramirez et al., 2014; Li et al., 2016). Compared with the traditional water vapor observations, ground-based GPS water vapor measurement has the advantages of high accuracy, high spatial-temporal resolution, all-weather availability, and low-cost (Haase et al., 2003; Pacione and Vespe, 2008; Lee et al., 2010; Means, 2013; Lu et al., 2015). Ground-based GPS water vapor products, mainly including precipitable water vapor (PWV), are widely used in many fields such as real-time vapor monitoring, weather and climate research, and numerical weather prediction (NWP) (Van Baelen and Penide, 2009; Karabatic et al., 2011; Rohm et al., 2014; Adams et al., 2017).

GPS observations require some kinds of meteorological elements to estimate PWV. Zenith hydrostatic delay (ZHD) can be calculated using surface pressure P_s by equation (Ning et al., 2013) :

$$ZHD = \left(2.2767 \pm 0.0015\right)\frac{P_s}{f\left(\varphi, H\right)} \tag{1}$$

where φ is the latitude, H is the geoid height in meters, and

$$f\left(\lambda, H\right) = \left(1 - 2.66\times10^{-3}\cos\varphi - 2.8\times10^{-7}H\right) \tag{2}$$

Then, zenith wet delay (ZWD) is generated by deducting ZHD from zenith total delay (ZTD). ZTD can be directly estimated from precise GPS data processing. Finally, a conversion factor Q, which is used to map ZWD onto PWV, is determined by the water-vapor-weighted mean temperature T_m over a GPS station. The mapping function from ZWD to PWV is expressed as (Bevis et al., 1992):

$$PWV = \frac{ZWD}{Q} = \frac{ZTD - ZHD}{Q} \tag{3}$$

and Q is computed using following formula:

$$Q = 10^{-6} \rho_w R_v \left[\left(k_3 / T_m \right) + k_2' \right] \tag{4}$$

where ρ_w is the density of liquid water, R_v is the specific gas constant for water vapor, $k_2' = (22.1 \pm 2.2)\mathrm{K} \cdot \mathrm{mbar}^{-1}$ and $k_3 = (3.739 \pm 0.012) \times 10^5 \mathrm{K}^2 \cdot \mathrm{mbar}^{-1}$ are physical constants (Ning et al., 2016) .

There are three main approaches to estimate T_m. They have respective advantages and disadvantages when they are applied for different purposes:

(1) The integration of vertical temperature and humidity profiles are believed to be the most accurate method. The profile data can be extracted from radio soundings or NWP datasets (Wang et al., 2016). However, some inconveniences have to be endured. It usually takes considerable amounts time to acquire the NWP data, which is normally released with large volumes every 6 hours. This limits the use of NWP data in the near real-time GPS-PWV retrieving. Radiosonde data is another profile data source, but it has low spatial and temporal resolution. At most of the radiosonde sites, sounding balloons are daily cast at 00:00 UTC and 12:00 UTC. Furthermore, a large amount of GPS stations are not located close enough to the radio sounding sites. Therefore, such methods are appropriate for the climate research or the study of long-term PWV trends, but do not meet the real-time requirements.

(2) Several global empirical models of T_m are established based on the analyses of T_m time series from NWP datasets or other sources (Yao et al., 2012; Chen et al., 2014; Bohm et al., 2015). T_m at any time and any location can be estimated from these models. They are often independent of the current meteorological observations which are required to be observed together with the GPS data. However, some important real variations, which may be dramatic during some extreme weather events, can be lost without the constraints of current real data (Jiang et al., 2016). Therefore, these modeled estimates are not accurate enough for high-precision meteorological applications, such as providing GPS-PWV estimates for weather prediction.

(3) Many studies indicated that T_m parameter has relationship with some surface meteorological elements, such as surface

air temperature or surface air humidity (Bevis et al., 1992; Yao et al., 2014a). These surface meteorological parameters can be measured accurately and rapidly. T_m is then estimated using these surface measurements. However, these studies also revealed that the relationships are often weak, except the T_s-T_m relationship. For example, Bevis introduced the Bevis T_s-T_m equation, T_m=0.72 T_s+70.2 [K], according to analyzing 8712 radiosonde profiles collected at 13 sites in the U.S. over two years (Bevis et al., 1992). This equation has been widely used in many other studies.

According to Rohm's research (Rohm et al., 2014), GPS-ZTD can be estimated very precisely by real-time GPS data processing. This means that T_m is one of the key parameters in the near real-time GPS-PWV estimation. On the other hand, method (3) is the most suitable method for estimating T_m in near real-time because of its balance between timeliness and accuracy. The T_s-T_m relationship has spatial-temporal variations. Several regional T_s-T_m equations were established using the profile data over corresponding fields (Wang et al., 2012). However, it is not precise enough to apply the same T_s-T_m model over a vast field, e.g., in the Indian region (Singh et al., 2014). Aside from this, some vast areas have no specific high-precision T_s-T_m model, for example over the oceans. In general, significant differences exist between oceanic and terrestrial atmospheric properties, especially near the surface layer and within the boundary layer. The change of T_s from land to ocean may be very different from that of T_m. Therefore it is necessary to model the T_s-T_m relationship over oceanic regions, since several ocean-based GPS meteorology experiments demonstrated the potential of such technique to retrieve PWV over the broad ocean (Rocken et al., 2005; Kealy et al., 2012). A global gridded T_s-T_m model has been established in Lan's study (Lan et al., 2016). In Lan's model, the 2.0° × 2.5° T_m data from "GGOS Atmosphere" and the 0.75° × 0.75° T_s data from the European Centre for Medium-Range Weather Forecasts (ECMWF) reanalysis data are both smoothed to the resolution of 4° × 5°. Actually the T_s-T_m relationship has time variation (Yao et al., 2014a). However, Lan's model is static and does not consider the time variation.

The objective of this study is mainly to (1) develop global gridded T_s-T_m models without any smoothing of the data, then assess their precision, and (2) study the performances of GPS-PWV retrievals using our T_s-T_m models. Table (1) lists the main differences between the T_s-T_m model developed in this study and the other global used T_m models. In section 2, the data sources and determining methods of T_m are introduced in detail. Then, in section 3 we analyze the T_s-T_m relationships and their variations on a global scale. Global-gridded T_s-T_m estimating models in different forms are established and evaluated in section 4. Section 5 compares different PWV retrievals and section 6 presents conclusions based on our experiments.

Table 1. Main differences between T_s-T_m models developed in this study and other global used T_m estimation models

Strategies \ T_s-T_m Models	Bevis model (Bevis et al., 1992)	Latitude-related linear model (Yao et al., 2014b)	Global-gridded model (Lan et al., 2016)	Time-varying global gridded model (our study)	GPT2w model (Bohm et al., 2015)
Applicable Regions	Regional/Global	Global	Global	Global	Global
Data Sources	Radiosonde	T_s from the 0.75° × 0.75° ERA-Interim, and T_m from the 2° × 2.5° "GGOS Atmosphere"	T_s from the 0.75° × 0.75° ERA-Interim , and T_m from the 2° × 2.5° "GGOS Atmosphere"	T_s and T_m both from the 0.75° × 0.75° ERA-Interim	T_m from the 1° × 1° ERA-Interim monthly mean data
Data Processing	Integrate radiosonde profiles	4° × 5° Sliding window smooth	4° × 5° Sliding window smooth	Integrate ERA-Interim profiles	Integrate ERA-Interim profiles
Variations in model	Static without any variations	Spatial variations depend on only latitude(15° latitude interval), but no temporal variations	4° × 5° global gridded, but no temporal variations	0.75° × 0.75° global gridded and considering time variations	1° × 1° global gridded, considering time variations, but independent of current surface observations

2. Data Sources and Methodology

2.1 T_m Definition

T_m is defined as a function related to the temperature and water vapor pressure. It can be approximated as the following formula (Bevis et al., 1992):

$$T_m = \frac{\int \frac{e}{T} dz}{\int \frac{e}{T^2} dz} \approx \frac{\sum_{i=1}^{n} \frac{e_i}{T_i} \Delta z_i}{\sum_{i=1}^{n} \frac{e_i}{T_i^2} \Delta z_i} \tag{5}$$

where e and T respectively represent vapor pressure in hPa and temperature in Kelvin, i denotes the ith pressure level and Δz_i is the height difference of ith levels . Vapor pressure e is calculated using equation $e=e_s \times RH$; RH is the relative humidity, and the saturation vapor pressure e_s can be estimated from the temperature observations using Goff-Gratch formula (Sheng et al., 2013). For the ith level, e_i parameter at the middle height is calculated by vertically exponential interpolation of its two neighbor measurement points' water vapor pressure. The temperature is estimated by linear interpolation of the two neighbor temperatures. The integral intervals are from the earth's surface to the top level of the profile data. The height of the top level depends on the data sources we employed, which will be shown in section 2.2.

2.2 Data sources and Methodology of T_m Determination

Equation (5) needs temperature, height and relative humidity values through the entire atmospheric column. The essential profile data can be obtained from the radiosondes or NWP datasets.

We employed radiosonde data from the Integrated Global Radiosonde Archive (IGRA, ftp://ftp.ncdc.noaa.gov/pub/data/igra) to calculate T_m. Version 2.0 of the IGRA-derived sounding parameters provides pressure, geopotential height, temperature, saturation vapor pressure, and relative humidity observations at the observed levels. Bias may be introduced if the integrals were terminated at lower levels (Wang et al., 2005), thus the integrations were performed up to the topmost valid radiosonde data. According to our quality control processes, some radiosonde profile data were rejected. In each profile, the surface observations must be available and the top profile level should not be lower than 300 hPa standard level. Furthermore, the level number between the surface and the top level should be greater than 10 to avoid too sparse vertical profile. At most of the radio sounding stations, sounding balloons are launched every 12 hours, and their ascending paths are assumed to be vertical.

Profile data are usually provided by NWP products at certain vertical levels. The ERA-Interim product from ECMWF provides data on a regular 512 longitude by 256 latitude N128 Gaussian grid after the grid transforming performed by the NCAR's Data Support Section (DSS). On each grid node of ERA-Interim, temperature, relative humidity and geopotential at 37 isobaric levels from 1000 hPa to 1 hPa can be obtained. Dividing the geopotential by constant gravitational acceleration value ($g \approx 9.80655$ m/s^2), we can determine the geopotential heights of the surface and levels. Datasets are available at 00:00, 06:00, 12:00 and 18:00 UTC every day and have been covering a period from 1979.01 to present.

In theory, the computation of equation (5) should be integrated through the entire atmospheric column, and the geopotential height should be converted to the geometric height. However, water vapor is solely concentrated in the troposphere, and most of it is specifically located within the first 3 kilometers above sea-level. Moreover, in the two selected datasets, the geopotential heights of top pressure levels are approximately 30~40 km. Geopotential height is very close to geometric height in such height ranges. According to our computation, the relative difference between them is only between 0.1 %~0.9 %. In fact, the height difference Δz can be replaced by the geopotential height difference Δh in equation (5), since the division operation can almost eliminate the difference between the two different height types. The T_m value nearly has no change after such height replacement. For the convenience of calculations, we directly employed the geopotential height variable. In this paper, we denoted the T_m derived from ERA-Interim as T_{m_ERAI}.

At each reanalysis grid node, the computation of equation (5) always starts from the surface height to the top pressure level. The pressure levels below surface height were rejected in the calculation. T_s is defined as the variable of "temperature at 2 meters above ground", and surface water vapor pressure can be derived from the "2 meter dewpoint temperature" variable in ERA-Interim. These T_s were also used in the regression analyses between T_m and T_s.

3. Correlation between Ts and Tm

Many studies have indicated the close relationship between T_s and T_m. However, T_m is also found to not be closely related to T_s in some regions, e.g., in the Indian zone (Raju et al., 2007). Using the T_m and T_s generated from the global gridded reanalysis data, we are able to study the T_s-T_m relationship in detail.

We first carried out a linear regression analysis on the four years long T_s and T_m data generated from the point radiosonde data and the global gridded ERA-Interim datasets. The data cover the period from 2009.01 to 2012.12. The analysis results are shown in figure (1). Although the two datasets have different temporal resolutions (12 hours for the radiosonde data and 6 hours for the ERA-Interim data) and spatial resolutions, both analyses agree with each other. This is expected because the radiosonde data have been assimilated into the ERA-Interim products. Our analyses also indicate that the T_s-T_m correlation coefficient is generally related to the latitude. The same conclusion has been drawn in other studies (Yao et al., 2014b). Significant positive correlation coefficients can be found in the mid- and high- latitudes and reaches the maximum in the Polar Regions. Then, the correlation coefficients drop dramatically in the low latitudes. We further analyzed the main reason for these changes. T_m variable in the low latitudes is stable, thus it shows independence of the other parameters. To study the variations of T_s and T_m, we illustrated the denary logarithm values of their standard deviations in figure (2). It is evident that T_m varies to a lesser degree in the low latitudes. Aside from the latitude-related features, there are obvious differences of the T_s-T_m correlation coefficient between land and ocean. Analyses even demonstrate negative correlation coefficients over certain oceans, e.g., low-latitude Western Pacific, Bay of Bengal or Arabian Sea. Unreliable regression analysis results may be derived when the T_s and T_m data both have small variations. In figure (3), scatter plots of T_s and T_m from ERA-Interim at two locations N 0.35° E 180.00° and N 70.53° E 180.00° are given. As the blue dots show, the T_s-T_m relationship is weak in the areas near the equator. It is because that the entire variation ranges of T_s and T_m are both below 10 K. As the magenta line shows, the linear regression result also makes less sense. The T_s-T_m correlation coefficient is only -0.0893. Other than the large spatial variations, studies have revealed that T_s-T_m relationships also have temporal variations (Wang et al., 2005). Therefore, a good T_s-T_m model should take both the spatial and temporal variations into consideration, and this is the main aim in the following sections.

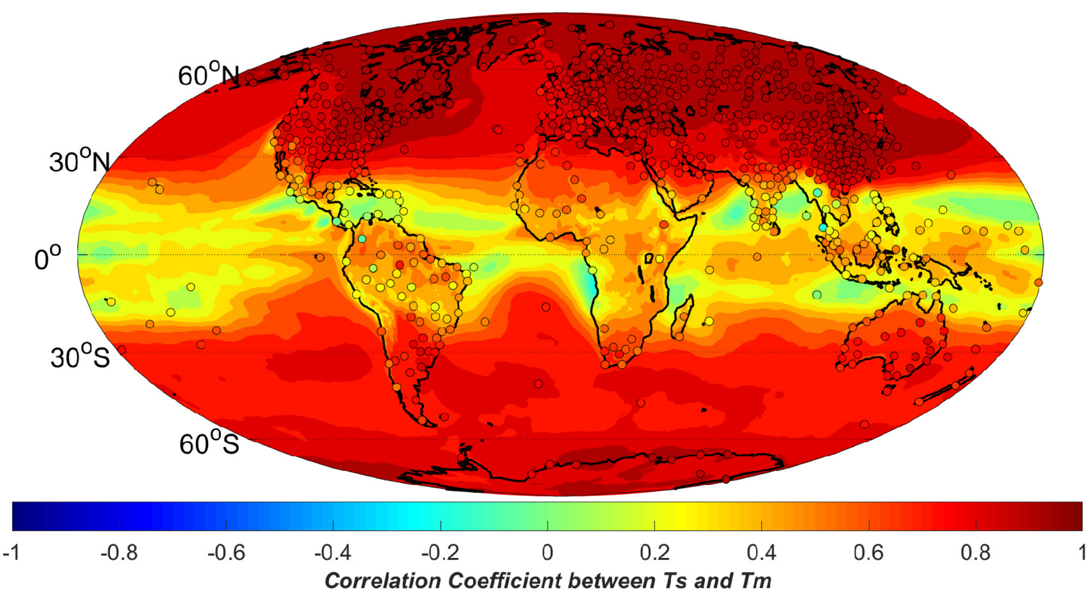

Figure 1: Correlation coefficients between T_s and T_m generated from radiosonde data (dots) and ERA-Interim reanalysis datasets (color-filled contours) over a period of 4 years from 2009 to 2012.

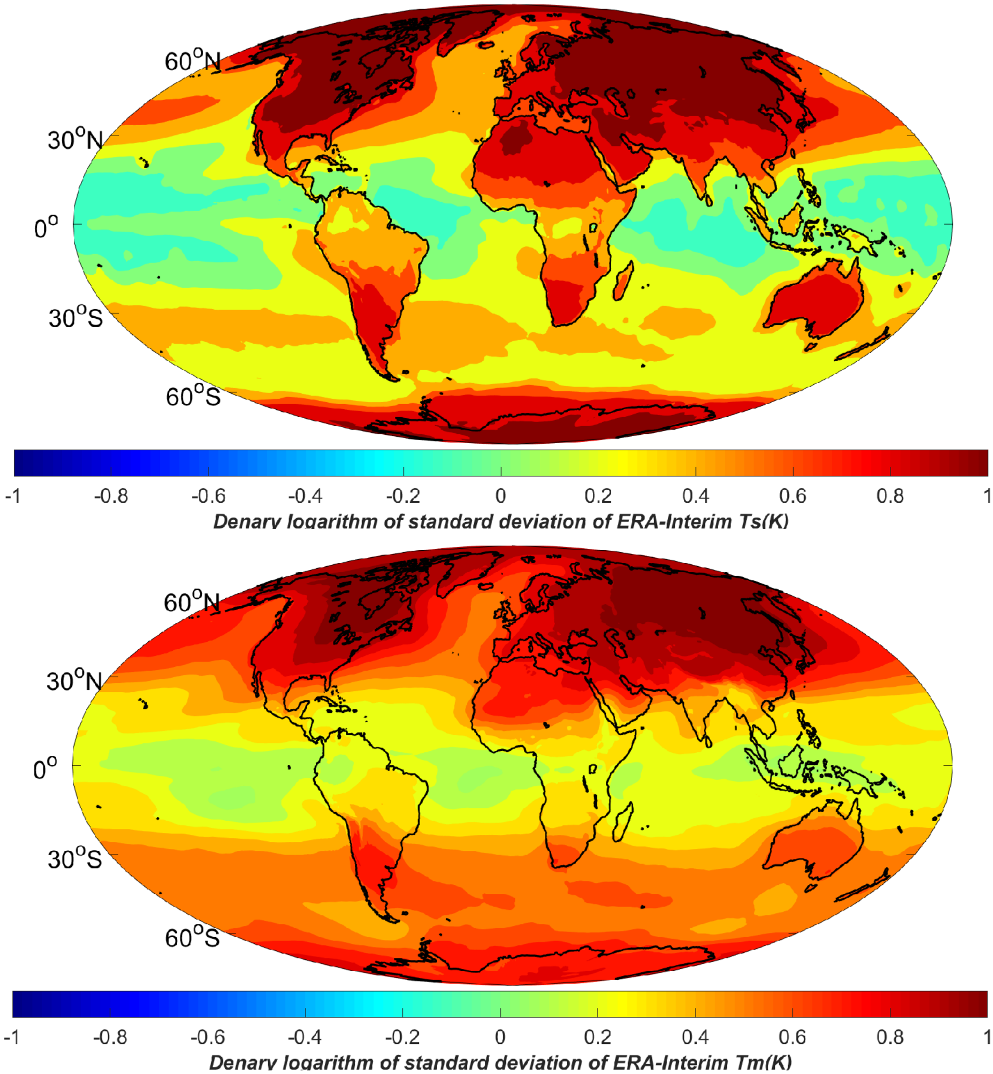

Figure 2: Denary logarithm of the standard deviation of (top) T_s and (bottom) T_m generated from the ERA-Interim over a period of 4 years from 2009 to 2012. Temperature unit is Kelvin.

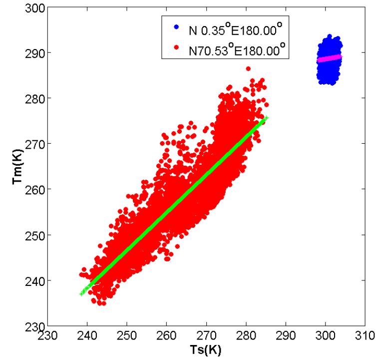

Figure 3: T_s-T_m scatter plots at two locations: (blue dots) N 0.35° E 180.00° and (red dots) N 70.53° E 180.00°, the magenta and green lines are their linear fitting curves. Temperature unit is Kelvin.

4. Developments of Global-gridded T_s-T_m models

Since the T_s-T_m relationship has large spatial variations, it is necessary to establish detailed global gridded T_s-T_m estimating equations for precise GPS-PWV estimations. In this section, a static global gridded model and a time-varying global gridded model are established and assessed.

4.1 Static global-gridded T_s-T_m model

Linear formula expressed as $T_m = aT_s + b$ has been adopted in many studies. Based on the T_s and T_m products from ERA-Interim, we performed linear fittings of T_s versus T_m on each grid point. Then, the slope constant (a), the intercept constant (b) and the fitting root mean square error (RMSE) of each linear expression were calculated and contoured in figure (4). The a and b values are related to the latitude as well as the underlying surface. In the mid-high latitudes over the northern hemisphere, constant a value varies from 0.6 to 0.8, and constant b is approximately 100~50 over most of the continents. The constants in the Bevis equation are within these value ranges. Constant a is smaller (approximately 0.5~0.7) over the lands in the mid-high latitudes over the southern hemisphere. Especially, there are acute value changes of constant a and b from land to ocean in the mid-high latitudes. The reason for this is the different variation features of T_s and T_m, which can be seen in figure (2). In the low latitudes, a value is smaller than the other regions. This is because of the low variations of T_s and T_m. The fitting RMSE are within 2~4 K over the mid-high latitude lands, and relatively lower values over the oceans or the low latitudes. The reason for the low RMSE around the equator is the smaller fluctuations of T_m. Meanwhile, there is no RMSE larger than 4.5 K in the results of our model. The precision and the resolution of our static model is clearly better than previous models (Lan et al., 2016). It is because that we performed no spatial or temporal smoothing of the data during the data processing.

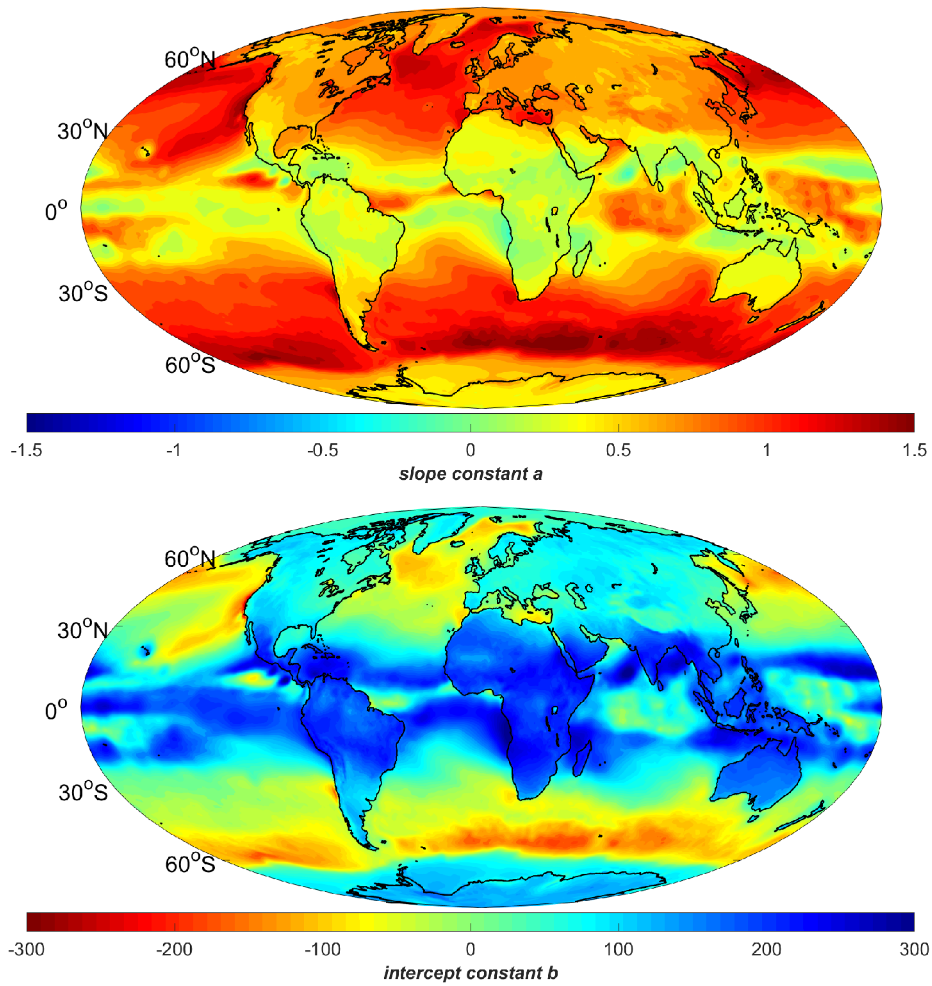

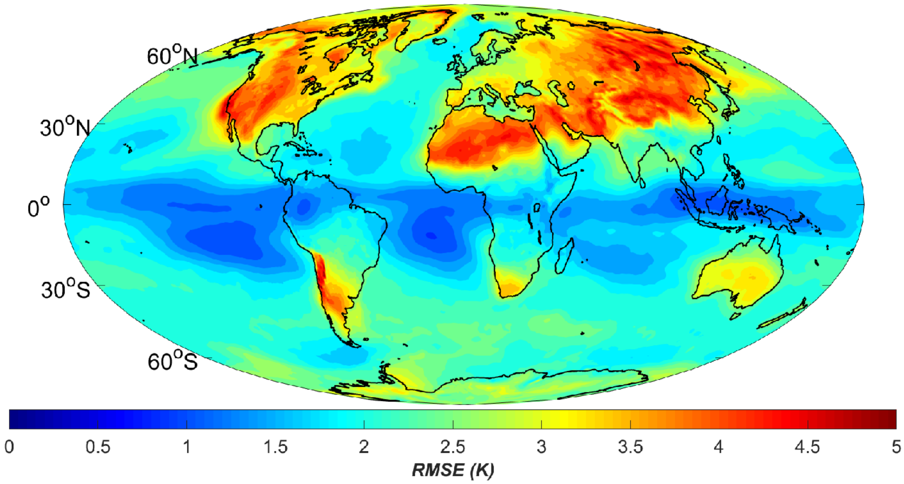

Figure 4: Distribution of the (top) slope constant *a*, (middle) intercept constant *b*, and (bottom) RMSE of static linear T_s-T_m equations at ERA-Interim grid nodes. Temperature unit is Kelvin.

4.2 Time-varying global-gridded T_s-T_m model

The T_s-T_m relationship has time variations which should also be considered in the precise T_s-T_m model. Therefore, a time-varying equation is applied for T_s-T_m regression at each grid node:

$$T_m = aT_s + b + m_1 \cos\left(\frac{doy}{365.25}2\pi\right) + m_2 \sin\left(\frac{doy}{365.25}2\pi\right) + n_1 \cos\left(\frac{doy}{365.25}4\pi\right) + n_2 \sin\left(\frac{doy}{365.25}4\pi\right) + p_1 \cos\left(\frac{hr}{12}\pi\right) + p_2 \sin\left(\frac{hr}{12}\pi\right) \tag{6}$$

where *doy* represents the observed day of year and *hr* is the observed hour in UTC time; (m_1, m_2), (n_1, n_2) and (p_1, p_2) are the fitting coefficients of corresponding formula items. These formula items can reflect the amplitudes of annual, semiannual and diurnal variations in our T_s-T_m models.

Our regression indicate that the static terms in equation (6), which are determined by the coefficients *a* and *b*, are similar to the static models in section 4.1 except some differences over the oceans. Other than *a* and *b*, we also illustrated the amplitudes of annual, semiannual, and diurnal terms. We can see that there are large annual variations (amplitude > 5 K) in the vast regions from Tibet to North Africa, and in some places of the Siberia and Chile. Large diurnal variations (amplitude > 3 K) mainly occur in the mid-latitude lands such as Northeast Asia or North America. Semiannual variations, however, are small in most of areas except some high-latitudes (amplitude > 3 K). All variations are smaller over the oceans due to the slower temperature changes over the waters than the lands. The estimated T_m's RMSE is also contoured in figure (5), and we can see that the RMSE dropped significantly in the regions with large annual or diurnal variations.

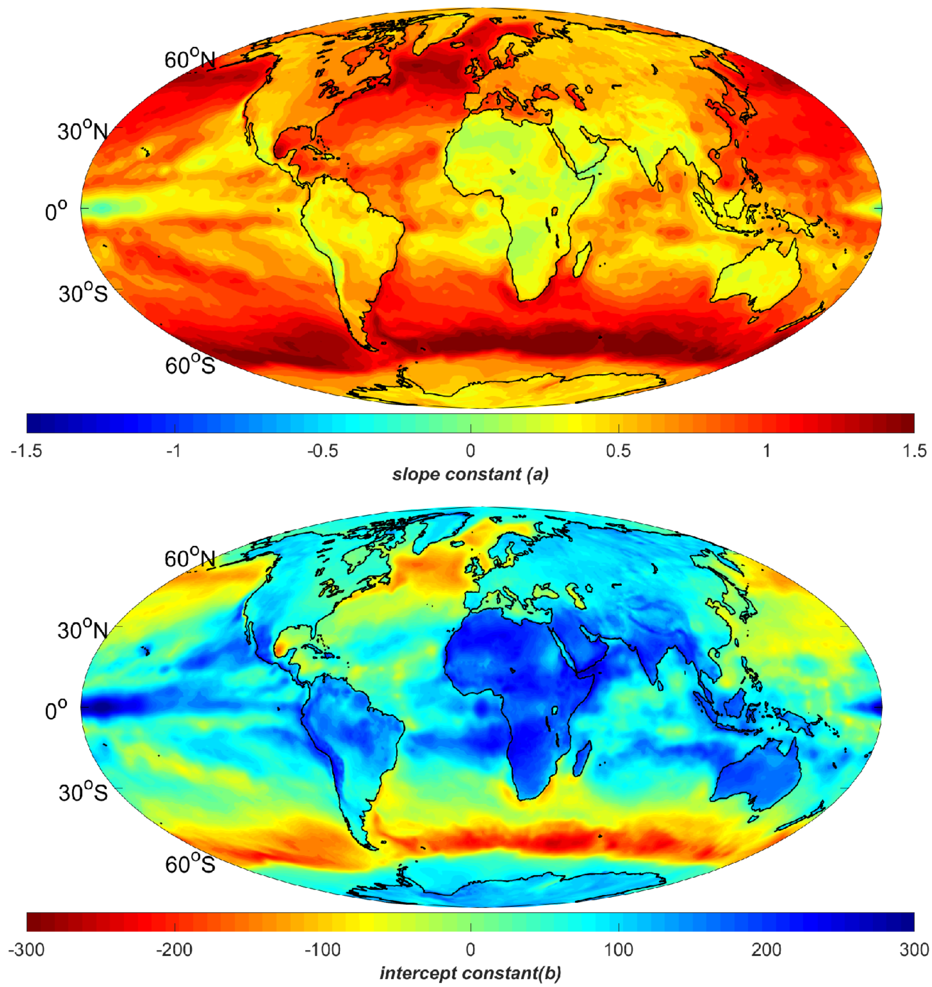

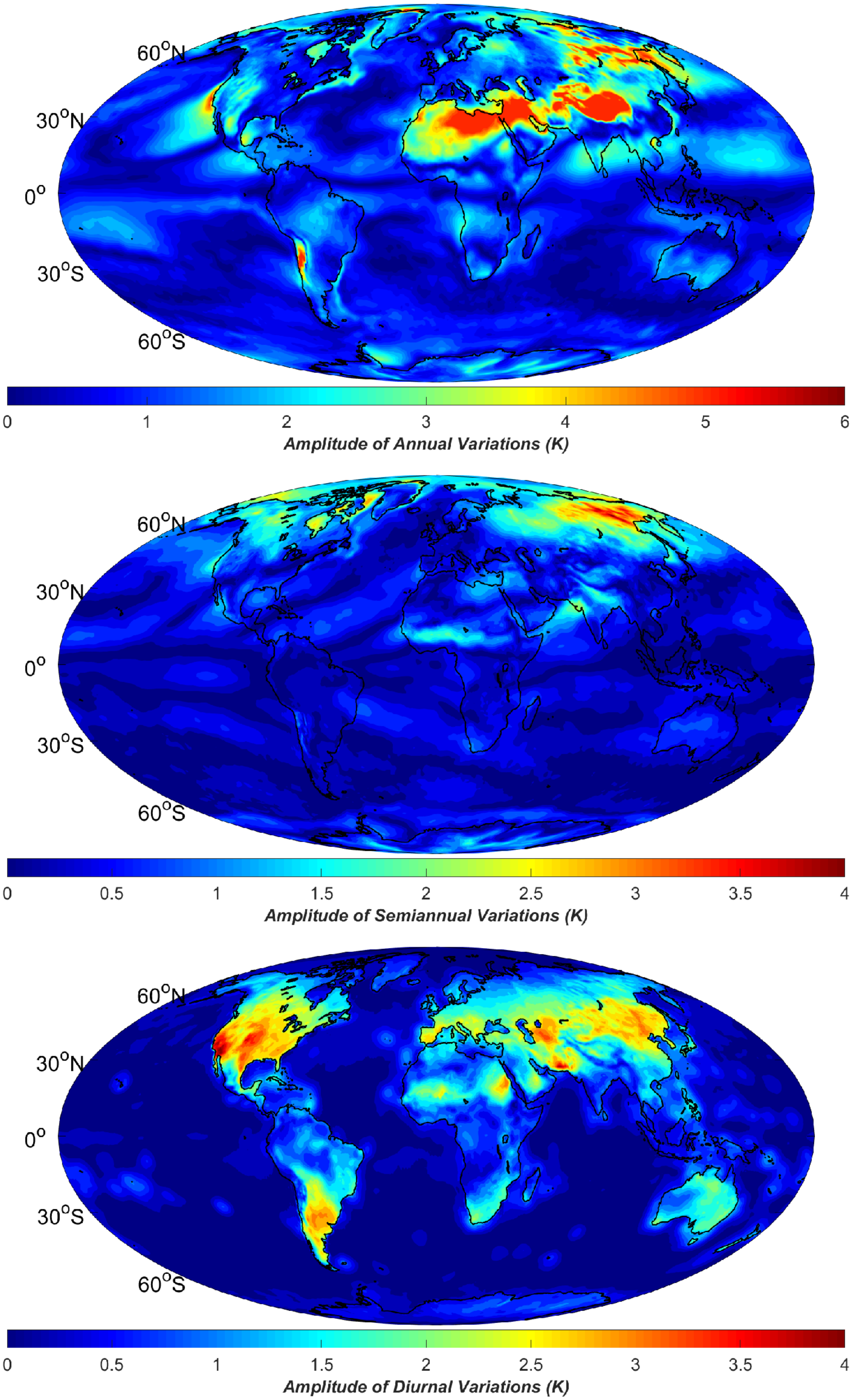
60°N
30°N
0°
30°S
60°S
0 1 2 3 4 5 6
Amplitude of Annual Variations (K)
60°N
30°N
0°
30°S
60°S
0 0.5 1 1.5 2 2.5 3 3.5 4
Amplitude of Semiannual Variations (K)
60°N
30°N
0°
30°S
60°S
0 0.5 1 1.5 2 2.5 3 3.5 4
Amplitude of Diurnal Variations (K)

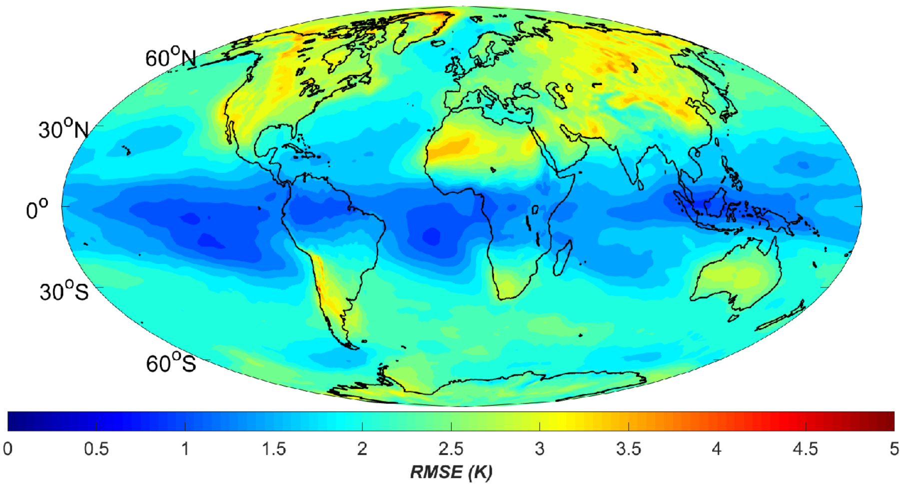

Figure 5: （top）The slope constant *a*, (second) intercept constant *b*, amplitudes of T_m (third) annual, (forth) semiannual and (fifth)diurnal terms in our time-varying global gridded T_s -T_m model, and (bottom) the model estimated T_m 's RMSE distribution. Temperature unit is Kelvin.

4.3 Assessments of T_s-T_m models

To assess the precision of the T_s-T_m models further using other independent data sources, we generated T_m and T_s from the radiosonde data at 723 radiosonde stations in the year 2016. These data are not assimilated into the 2009~2012 ERA-Interim datasets. As a result, we can regard them as independent data to our model. At each radiosonde site, different T_s-T_m models were employed to calculate T_m. In addition, we also estimated T_m using the 1° × 1° GPT2w model (Bohm et al., 2015), which is a global gridded T_m empirical model independent of the surface meteorological observation data. Then, these calculated T_m will be evaluated by comparing them with the radiosonde's integrated T_m (denoted as T_{m_RS}) twice a day.

The model estimations of T_m are denoted as T_{m_Bevis}, T_{m_LatR}, T_{m_static}, $T_{m\_varying}$, and T_{m_GPT2w} from the Bevis equation, Yao's latitude-related model, our static global gridded model, time-varying global gridded model, and the GPT2w model. When the global gridded models are employed, there is a problem that a radiosonde station may not be located at a grid node. Therefore, the coefficients in T_s-T_m equations should be horizontally interpolated from the neighboring grids to the radiosonde sites. The interpolation formula is expressed as (Jade and Vijayan, 2008) :

$$C_{site} = \sum_{i=1}^{4} w^i C_{grid}^i \tag{7}$$

C_{site} and C^{i}_{site} represent the coefficients in T_s-T_m equations at the radiosonde site location and its neighboring grids, respectively. w^i is the interpolation coefficients, which is determined using equation:

$$w^i = \frac{\left(R\psi^i\right)^{-\lambda}}{\sum_{j=1}^{4}\left(R\psi^j\right)^{-\lambda}} \tag{8}$$

where R=6378.17 km is the mean radius of the earth, λ is the scale factor which equals one in our study, and ψ^i is the angular distance between the ith grid node and the station's position. ψ^i is computed using following formula related to latitude φ and longitude θ:

$$\cos\psi_i = \sin\varphi_i \sin\varphi + \cos\varphi_i \cos\left(\theta_i - \theta\right)\cos\varphi \tag{9}$$

Considering the reanalysis grids are definite, and every radiosonde site is in situ; we can compute the interpolation coefficients in equation (5) for all of the radiosonde stations. Then, these coefficients are stored as constants to avoid reduplicating the calculation.

Taking T_{m_RS} as the reference values, we calculated the bias and RMSE of T_{m_Bevis}, T_{m_LatR}, T_{m_static}, $T_{m\_varying}$, and T_{m_GPT2w} at each radiosonde site. The results are illustrated in figure (6). Obviously in many regions, Bevis equation has bad precision with the absolute bias and RMSE are both larger than 5 K. T_{m_LatR} can reduce the estimated biases in many areas, but the RMSE remain large. Large biases still exist at quite a few radiosonde stations, e.g. in Africa or West Asia. T_{m_static} and T_{m_GPT2w} remove the large T_m biases at most of the radiosonde stations. $T_{m\_varying}$ performs significantly better over the world, especially in the Middle East, North America , Siberia region, etc.

Detailed statistics of the bias's and RMSE's distributions of different models are shown in figure (7) and table (2). At over 97.37 % of the radiosonde stations, the biases of $T_{m\_varying}$ are within -3~3 K. Large positive biases (> 3 K) nearly disappear in $T_{m\_varying}$. In contrast, there are significant large biases in T_{m_Bevis} and T_{m_LatR}. Improvements in RMSE are more evident. $T_{m\_varying}$'s RMSE are smaller than 4 K at over 91 % of the radiosonde sites, while few sites (<1 %) have RMSE larger than 5 K. This is clearly better than the other models. In T_{m_Bevis} and T_{m_LatR}, there are more than 17 % of the radiosonde sites have

RMSE larger than 5 K. The overall performance of T_{m_GPT2w} is very close to T_{m_Bevis}, except that its absolute bias is smaller than the other T_s-T_m models.

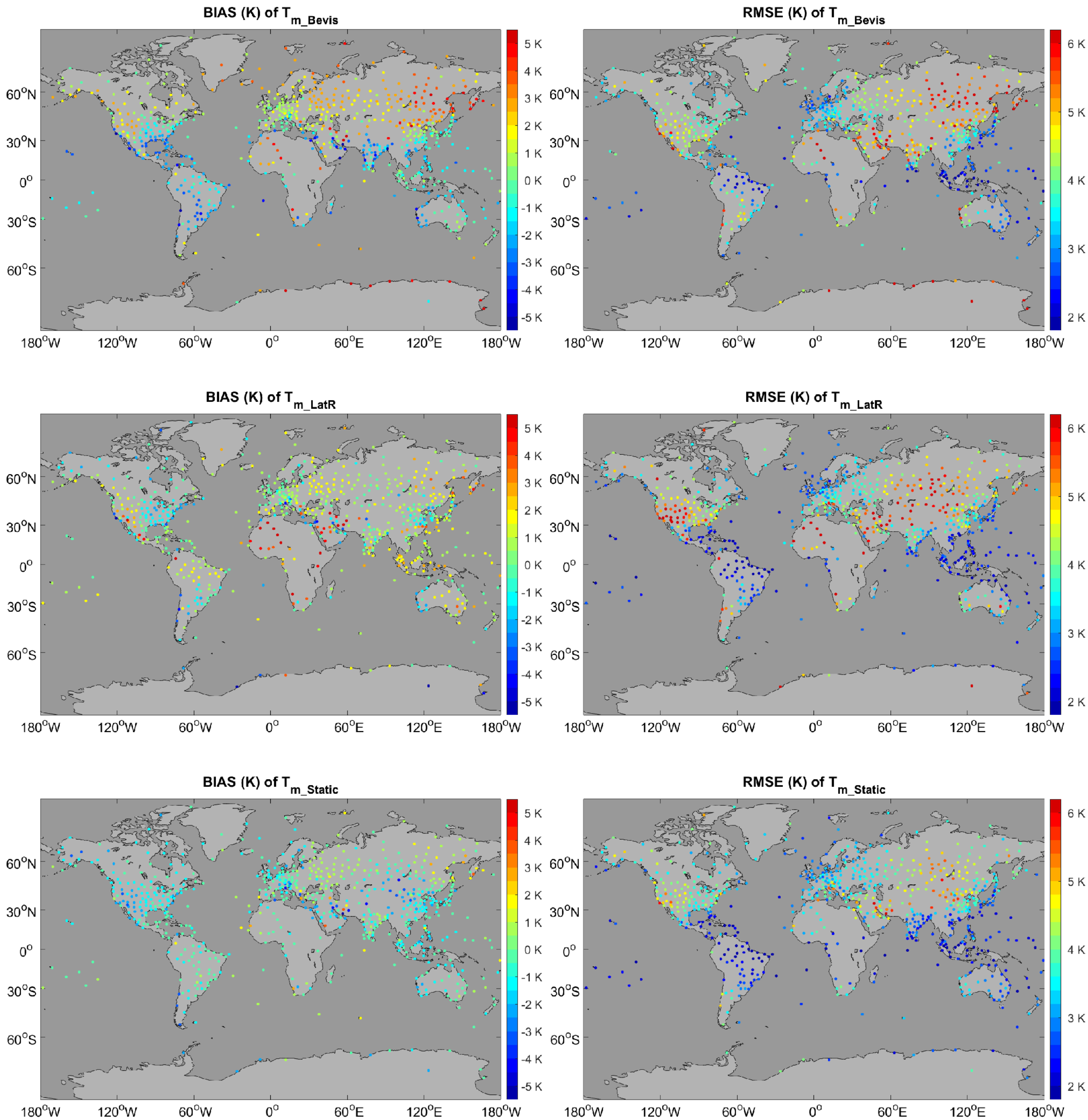

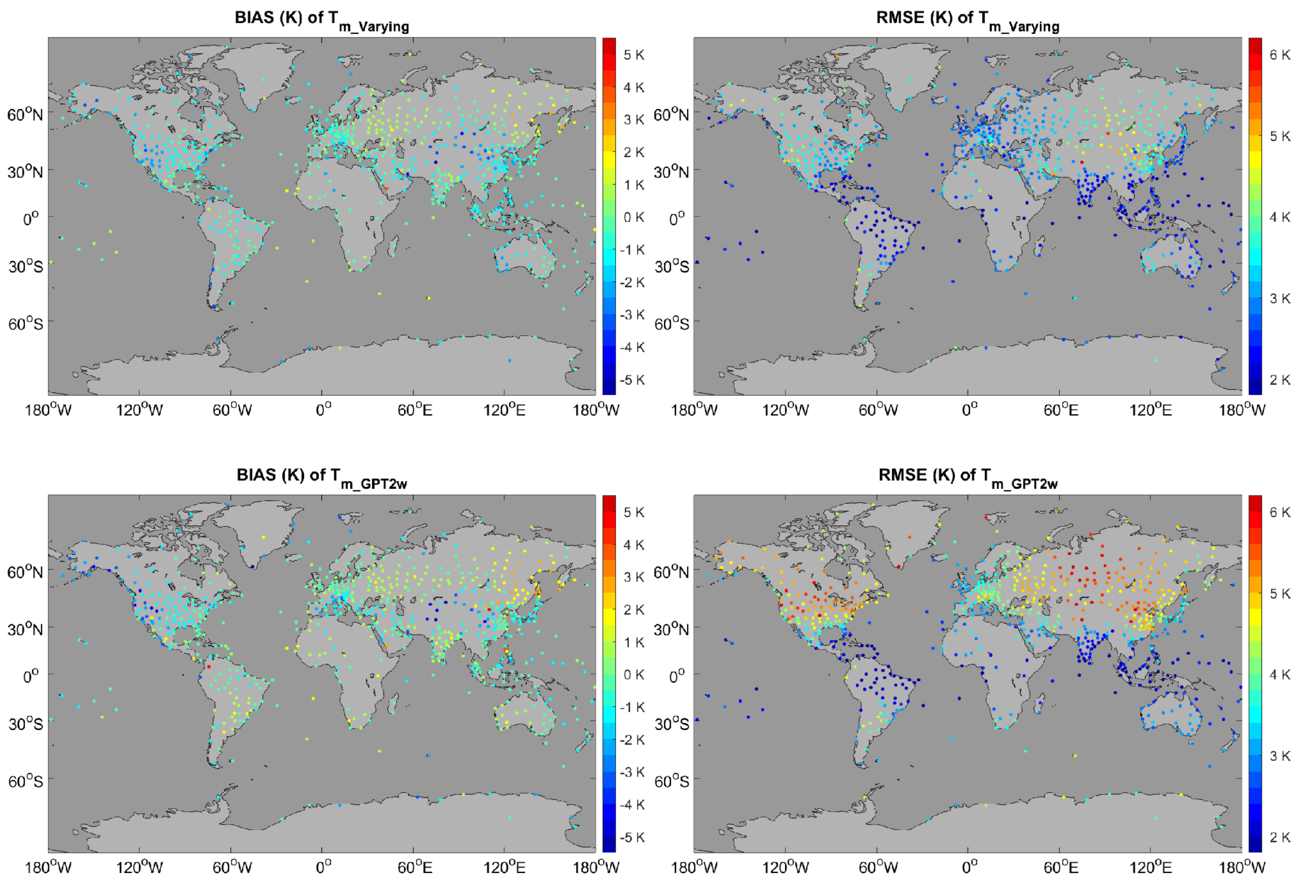

Figure 6: (left) The bias and (right) RMSE of the estimated T_m from (top) Bevis equation, (second) Yao's latitude-related model, (third) static global gridded model, (forth) time-varying global gridded model and (bottom) GPT2w model at each radiosonde station. Reference data are the radiosonde data of the year 2016. Temperature unit is Kelvin.

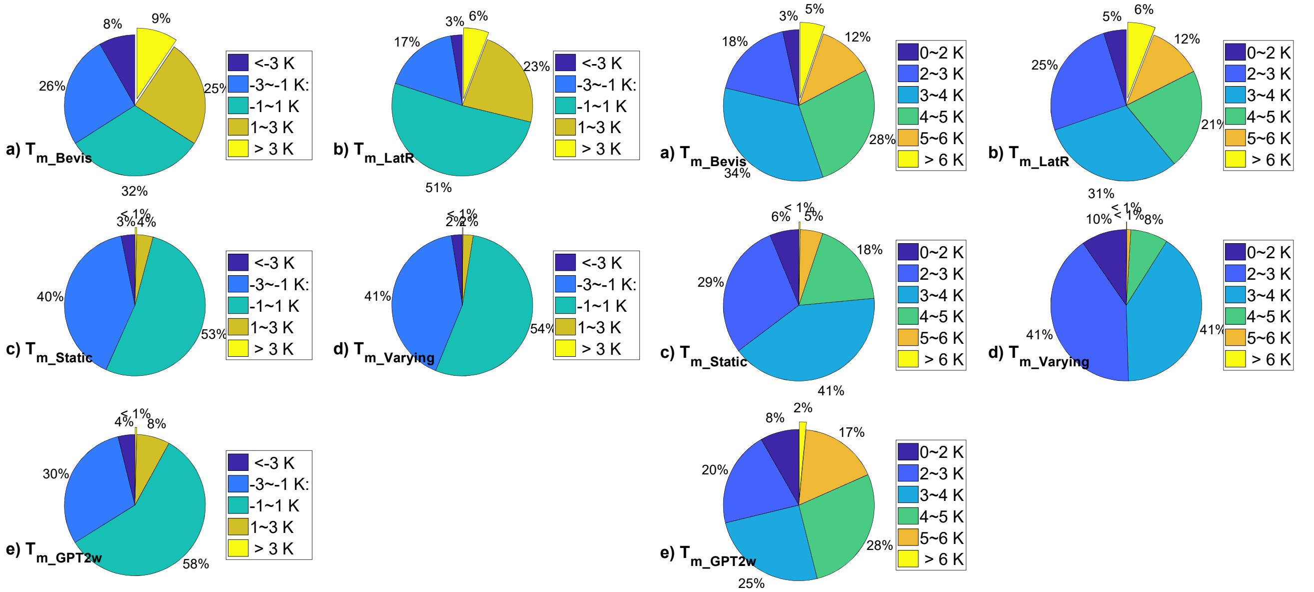

1) Bias distribution 2) RMSE distribution

Figure 7: (left) The bias's and (right) RMSE's distributions of T_{m_Bevis}, T_{m_LatR}, T_{m_static}, $T_{m\_varying}$ and T_{m_GPT2w} compared with the radiosonde data at 723 stations in the year 2016. Temperature unit is Kelvin.

Table 2: Statistics of T_m estimates from different models. Reference data are the radiosonde T_m derivations

Statistics	T_{m_Bevis}	T_{m_LatR}	T_{m_static}	$T_{m\_varying}$	T_{m_GPT2w}
Average value of absolute T_m bias (K)	1.88	1.30	1.13	1.08	1.06
Average value of T_m RMSE (K)	3.95	3.81	3.36	3.01	3.80
Average relative RMSE of T_m (%)	1.44	1.39	1.22	1.09	1.39
Max Relative RMSE of mean T_m (%)	3.69	4.26	2.40	2.19	4.31
% of sites with T_m RMSE < 4 K	55.19	61.00	76.49	91.01	53.94
% of sites with T_m Relative RMSE less than 1.5 %	59.47	64.73	78.01	89.76	56.43

To identify the superior T_m estimation model at each radiosonde site, we employed the following statistical tests under the assumption of normal distribution of the estimated T_m's error:

(1) First, Brown-Forsythe's tests (Brown and Forsythe, 1974) of equality of variances were carried out at each site for estimating the T_m errors from two different models, e.g., model ***A*** and ***B***. The purpose of this step is to determine whether there is significant variance difference between the T_m results. If the test rejects the null hypothesis at a 5 % significance level that the errors of model ***A*** and ***B*** have the same variance, the model with the smaller sample variance is regarded as the better one.

However, if the test does not reject the homogeneity of variances, analysis of variance (ANOVA) is performed in the next step.

(2) ANOVA is a technique used to analyze the differences among group means (Hogg, 1987). It evaluates the null hypothesis that the samples all have the same mean against the alternative that the means are not the same. If the null hypothesis is rejected at a 5 % significance level, the T_m sample with smaller absolute mean value is believed to be better. Otherwise, we think that two models perform almost the same at this radiosonde site.

(3) After multiple tests and comparisons, the best model at each radiosonde stations may be identified. However, at some sites no superior model can be confirmed. All the models are believed to have the equivalent performances.

Finally, we counted the number of sites at which each T_m model respectively performed the best. The results are given in table (3). The time-varying global gridded model is superior to the others at 434 radiosonde stations (60.03 % of all sites), while the second-best estimation, T_{m_GPT2w}, is superior at only 12.86 % of the sites.

Table 3: Number of radiosonde sites at which the five global applied T_m estimation models respectively perform superiorly

Superior model	**None**	T_{m_Bevis}	T_{m_LatR}	T_{m_static}	$T_{m\_varying}$	T_{m_GPT2w}
Number of sites	50	46	61	39	434	93

A comprehensive research on the uncertainty of GPS-PWV can be found in Ning's work (Ning et al., 2016). The uncertainties of the ZTD, ZHD and conversion factor Q have been studied in detail. The total uncertainty of GPS-derived PWV is:

$$\sigma_{PWV} = \frac{1}{Q}\sqrt{\sigma_{ZTD}^2 + \left(\frac{2.2767\sigma_{Ps}}{f(\varphi,H)}\right)^2 + \left(\frac{P_s\sigma_c}{f(\varphi,H)}\right)^2 + \left(PWV \cdot \sigma_Q\right)^2} \tag{10}$$

where σ_{PWV}, σ_{ZTD}, σ_{Ps}, and σ_Q are the uncertainty of the GPS-PWV, ZTD estimates, P_s observations and conversion factor Q, respectively. $\sigma_c = 0.0015$ denotes the uncertainty of the constant $C = 2.2767$ in equation (1), PWV is the GPS-PWV value and

$$\sigma_Q = 10^{-6}\rho_w R_v \sqrt{\left(\frac{\sigma_{k_3}}{T_m}\right)^2 + \sigma_{k_2'}^2 + \left(k_3 \frac{\sigma_{T_m}}{T_m^2}\right)^2} \tag{11}$$

where σ_{k_3}, $\sigma_{k_2'}$, and σ_{T_m} denote the uncertainty of the k_3, k_2' and T_m in equation (4).

Table 4: List of the uncertainty values for the error sources in GPS-PWV

Variables	σ_{ZTD} [mm]	σ_{Ps} [hPa]	σ_C	$\sigma_{k_2'}$ [K hPa^{-1}]	σ_{k_3} [$10^5 \times$ K^2 hPa^{-1}]
Uncertainty value	4	0.5	0.0015	2.2	0.012

However, Ning's study assumed the T_m were obtained from NWP models so the T_m's uncertainty was set to be small (σ_{T_m}=1.1 K). At each site, we replaced the σ_{T_m} by the T_m's RMSE shown in figure (6) to re-evaluate the σ_Q, while the other uncertainties are assumed to be the corresponding values listed in table (4) based on Ning's summaries. The σ_{Ps} equals 0.2 hPa in Ning's paper, however we enlarged it to 0.5 hPa in consideration of the possible worse performance of the surface barometers. The σ_Q in equation (11) was estimated using T_{m_Bevis}, T_{m_LatR}, T_{m_static}, $T_{m\_varying}$, and T_{m_GPT2w}, respectively. We also calculated the mean PWV and T_m values in equation (10) and (11). Then σ_{PWV} results were generated from the different σ_Q estimates using equation (10). Considering T_m's errors is propagated to Q, we calculated the percentage of σ_{PWV} caused by the uncertainty of Q (denoted as pQ). Larger pQ means more contribution of T_m's errors to the uncertainty of GPS-PWV. Comparisons between the $pQ_{Varying}$ (pQ estimated from $T_{m\_varying}$) and the other pQ estimates are illustrated in figure (8). Significantly $pQ_{Varying}$ is smaller than the pQ estimates from other T_m models at most of the sites. The pQ value grows with the PWV's increase, which can also be derived from equation (10). At some sites pQ drops more than 20 % from pQ_{Bevis} to $pQ_{Varying}$. It is evident that more precise T_m estimation model is effective to reduce the contribution of T_m error to the uncertainty of GPS-PWV.

It is worth mentioning that the uncertainty of ZHD may be underestimated in some situations. There are two reasons for this. Firstly, the calculation of ZHD assumes that the water vapor is not contributed to the mass of the atmosphere. The ZHD error introduced by this assumption is often negligible. But in some very wet regions, the mass of water vapor could produce significant errors to the ZHD calculation. Secondly and more importantly, the error of P_s in equation (1) can be very large sometime. From table (4) we can see that the σ_{Ps} is small, which is reasonable when the surface barometer is calibrated routinely and equipped together with the GPS antenna. However, if there were significant height difference between the GPS antenna and the barometer, the error of ZHD would increase significantly. Snajdrova (Snajdrova et al., 2006) found that 10 m of height difference approximately causes a difference of 3 mm in the ZHD . On the other hand, P_s can be generated from NWP data if there were no nearby barometer to GPS site. The error of P_s could be very large using this method (Means and Cayan, 2013; Jiang et al., 2016). In these cases, the GPS-PWV's error reduction due to the more precise T_m estimation will be very limited. When the σ_{Ps} is larger than 5 hPa, most of the pQ values are smaller than 10 %, while the error associated with the calculation of ZHD can contribute more than 80 % of the GPS-PWV's error.

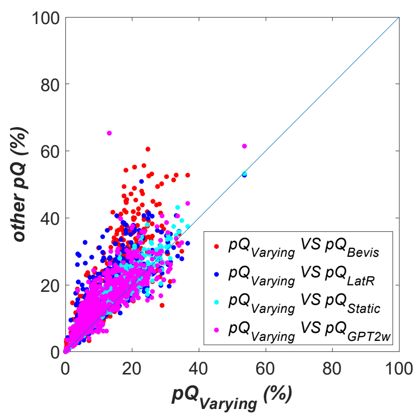

Figure 8: Comparisons between $pQ_{Varying}$ and the other pQs, where pQ represents the percentage of the uncertainty cause by conversion factor Q in total GPS PWV uncertainty.

In figure (9)，the T_m series at IGRA station NO.62378 (N 29.8628° E 31.3492°) are given. We can see that large negative biases (< -5 K) between T_{m_Bevis} (or T_{m_LatR}) and T_{m_RS} exist. T_{m_static} performs only slightly better from July to October. However, $T_{m\_varying}$ and T_{m_GPT2w} can eliminate most of the seasonal errors. Different properties of T_m series appear at another IGRA station NO.40841 (N 30.2500° E 56.9667°). Some observation data are missing, but we can still see that there are large positive differences (> 5 K) between T_{m_Bevis} (or T_{m_LatR}) and T_{m_RS} throughout the year. The biases of T_{m_static} are much smaller, but some large errors still appear in many months. The $T_{m\_varying}$, however, performs as well as at the NO.62378 IGRA station, with small biases and good capturing of T_m's variations. The time series of T_{m_GPT2w} are smooth so they cannot capture the large fluctuations of T_m time series, which causes its worse accuracy than $T_{m\_varying}$.

On the other hand, even $T_{m\_varying}$ have large differences from T_{m_RS} at a few IGRA stations. It is because that our fitting analyses were based on the T_m values derived from ERA-Interim profiles. The quality of ERA-Interim data can be very poor in the regions with sparse observation data (Itterly et al., 2018). Improvements on the reanalysis data should be performed in future.

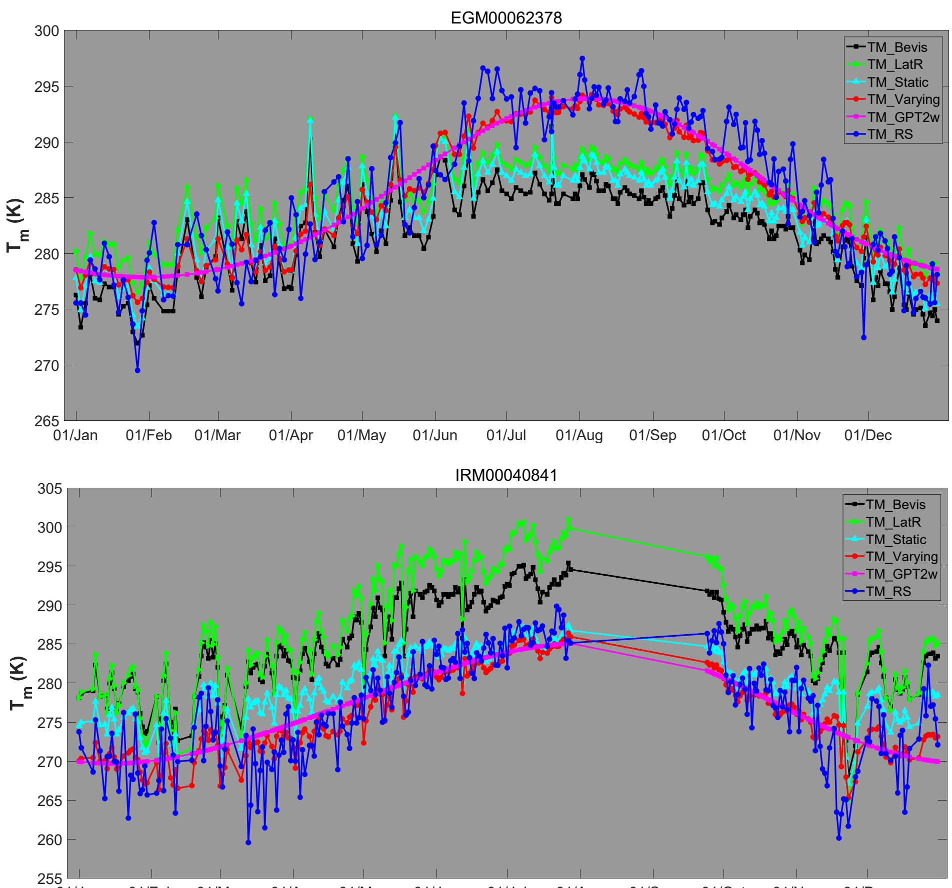

Figure 9: T_m series of T_{m_Bevis}, T_{m_LatR}, T_{m_static}, $T_{m\_varying}$, T_{m_GPT2w} and T_{m_RS} at (top) EGM00062378 and (bottom) IRM00040841 IGRA sites. Temperature unit is Kelvin.

5. GPS-PWV retrieving experiments

GPS-PWV has different error sources with different properties as described in section 4.3. It is complicated to evaluate GPS-PWV uncertainty due to the lack of collaborated additional independent techniques to monitor water vapor at the GPS site. Therefore, several experiments were carried out to investigate the GPS-PWV precision carefully.

5.1 Impact of T_m estimation

To study the impacts of T_m on the GPS-PWV retrievals, we first downloaded GPS ZTD products (Byun and Bar-Sever, 2009) at several IGS sites in the year 2016 from the CDDIS FTP address (ftp://cddis.gsfc.nasa.gov/pub/gps/products/troposphere/zpd). These selected GPS sites were equipped with meteorological sensors so the surface pressure and temperature measurements could also be obtained. ZHD was calculated using equation (1). It is deducted from ZTD to obtain ZWD. Then, T_m was generated through six approaches: the first five T_m series were T_{m_Bevis}, T_{m_LatR}, T_{m_static}, $T_{m\_varying}$, and T_{m_GPT2w}. The sixth T_m was integrated from the ERA-Interim profiles and interpolated to each GPS site (Jiang et al., 2016; Wang et al., 2016). Finally, the GPS-PWV was generated from the ZWD and the six different T_m estimates. We denoted these GPS-PWV sets as PWV_{BTm}, PWV_{LTm}, PWV_{STm}, PWV_{VTm}, PWV_{GTm}, and PWV_{ETm}. The only difference between these GPS-PWV estimations is the T_m estimation model; therefore, the impacts of other errors are excluded.

The T_m from ERA-Interim is believed to be the most accurate among our T_m estimates at the selected GPS sites. We regarded the PWV_{ETm} as reference values to assess the other PWV. Finally, the GPS-PWV at 74 IGS sites were obtained. Each GPS-PWV series have over one hundred compared points. The relative RMSE of PWV_{BTm}, PWV_{LTm}, PWV_{STm}, PWV_{VTm} and PWV_{GTm} at these selected stations were calculated and illustrated in figure (10). The detailed statistics are given in table (5). The mean relative error of all sites drops from 1.18 % of PWV_{BTm} to 0.91 % of PWV_{VTm}. At most of the sites, PWV_{VTm} has the minimum relative errors and is superior to the other PWV retrievals. PWV_{STm} and PWV_{VTm} obtain relative RMSE smaller than 1.0 % at 55 sites, while only 28 sites of PWV_{BTm}, 31 sites of PWV_{LTm} and 22 sites of PWV_{GTm} perform similarly. For example, at ALIC site which is located in Australia with mean PWV of approximately 23 mm, the relative RMSE dropped from 1.97 % of PWV_{BTm} to 1.10 % of PWV_{VTm}. The time series of the relative differences of PWV_{BTm}, PWV_{LTm}, PWV_{STm}, PWV_{VTm} , and PWV_{GTm} are given in figure (11). We found that some relative RMSE could reduce more than 2 % from PWV_{BTm}

to PWV_{VTm}. Obviously, PWV_{BTm} and PWV_{LTm} have larger relative errors throughout the year while the PWV differences are significantly larger only in the summer season. It is because that the T_m's variations in summer are not modeled well by both Bevis model and the latitude-related model. Furthermore, the higher PWV values in summer enlarge the PWV differences. PWV_{STm} eliminate those large differences but still retain some residual errors. These residuals are removed more than 1.0 mm in PWV_{VTm} further. PWV_{GTm} has some large errors during the period from May to July. All of these results demonstrate that our time-varying model has precision advantages.

Table 5: Statistics about the relative errors of different PWV retrievals

Statistics	PWV_{BTm}	PWV_{LTm}	PWV_{STm}	PWV_{VTm}	PWV_{GPT2w}
Mean relative RMSE of all sites	1.18 %	1.12 %	0.93 %	0.91 %	1.32 %
Number of sites with relative errors < 1.0 %	28	31	55	55	22

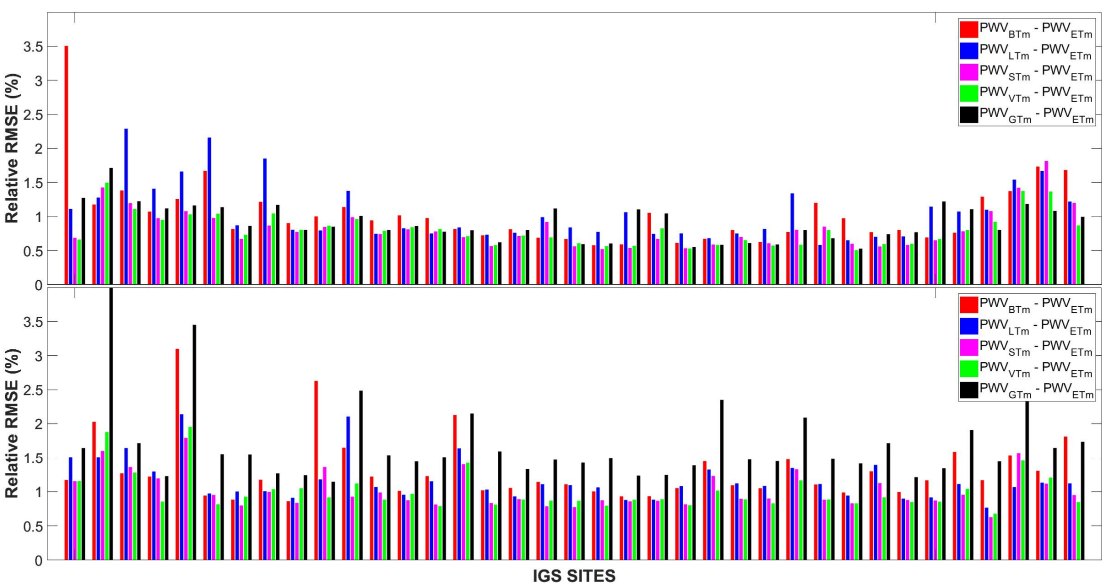

Figure 10: Relative RMSEs of PWV_{BTm}, PWV_{STm}, PWV_{VTm} and PWV_{GTm} compared with PWV_{ETm} at 74 IGS stations in the year 2016

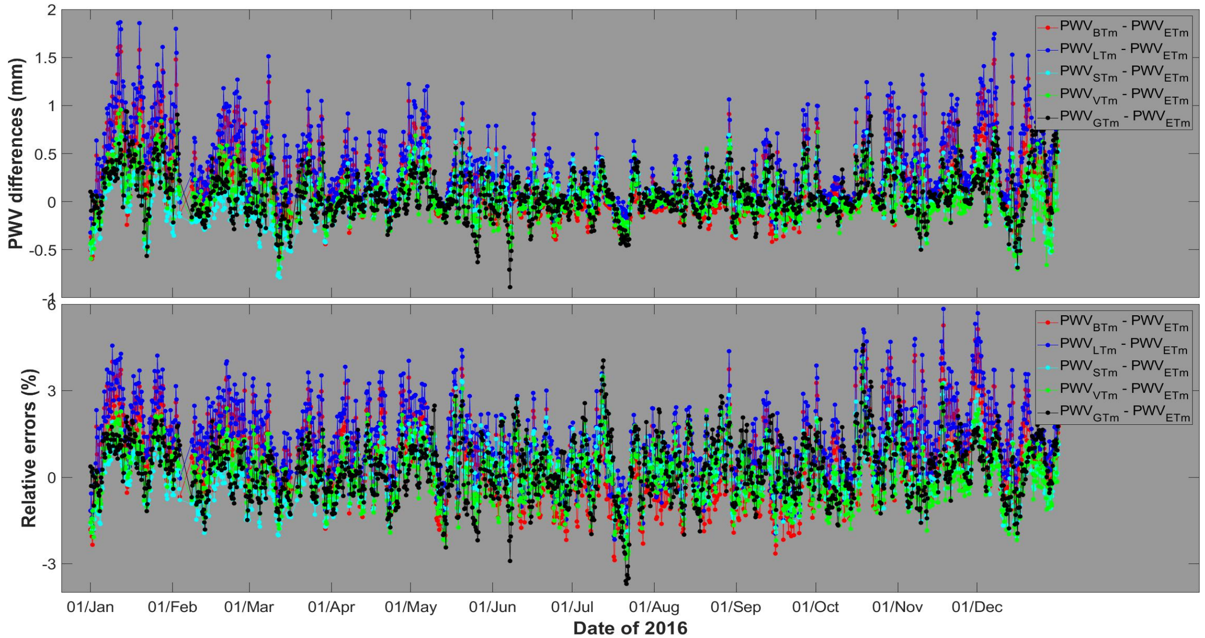

Figure 11: (top) PWV differences and (bottom) relative differences of PWV_{BTm}, PWV_{LTm}, PWV_{STm}, PWV_{VTM} and PWV_{GTm} compared with PWV_{ETm} at the ALIC station in the year 2016. PWV unit is mm.

5.2 Comparisons between GPS-PWV and radiosonde PWV

Among our selected 74 IGS sites, there are only 11 sites located within 5 km to the nearby IGRA radiosonde stations. At these common stations, we generated PWV from the radiosonde data (PWV_{RS}) by adjusting the sounding profiles to the heights of IGS sites. It worth noting that geoid undulation corrections should be carried out on each IGS site's geoid height (Jiang et al., 2016). Then, we compared PWV_{BTm}, PWV_{LTm}, PWV_{STm}, PWV_{VTm}, PWV_{GTm}, and PWV_{ETm} with PWV_{RS}. Figure (12) shows the statistics. The RMSE of GPS-PWV are approximately 1~5 mm. Comparisons indicate that the RMSE of different GPS-PWV retrievals are very close (differences < 0.2 mm) regardless of the applied T_m sources at most of the selected sites. This means that other errors (e.g. ZTD estimation errors or sounding sensors errors) instead of T_m occupied the differences between the GPS-PWV and the radiosonde PWV. Actually, each sounding does not represent the vertical sounding centered at the radiosonde site because of the complex path of the balloon. And GPS-PWV represents the averaged value of the water vapor zenithal projection from all the slant signal paths during the observation period. Such differences can introduce significant uncertainty to our comparisons. However, we still found obvious gaps between PWV at NRIL (N 88.3598° E 69.3618°, 4.1

km away from the NO.23078 radiosonde site). The RMSE decreases from 2.29 mm of PWV_{BTm} to 1.84mm of PWV_{VTm} and 1.42 mm of PWV_{ETm}. As shown in figure (13), the large PWV differences appear mainly from May to September. During those five months, mean GPS-PWV differences to PWV_{RS} decrease by over 30 % from 2.52 mm of PWV_{BTm} to 1.67 mm of PWV_{VTm}. Some differences can reduce 1~2 mm during the wetter months. The accuracy of PWV_{GTm} is close to PWV_{VTm} at this site, which indicates that the spatiotemporal variations of T_m are also modeled very well by GPT2w model.

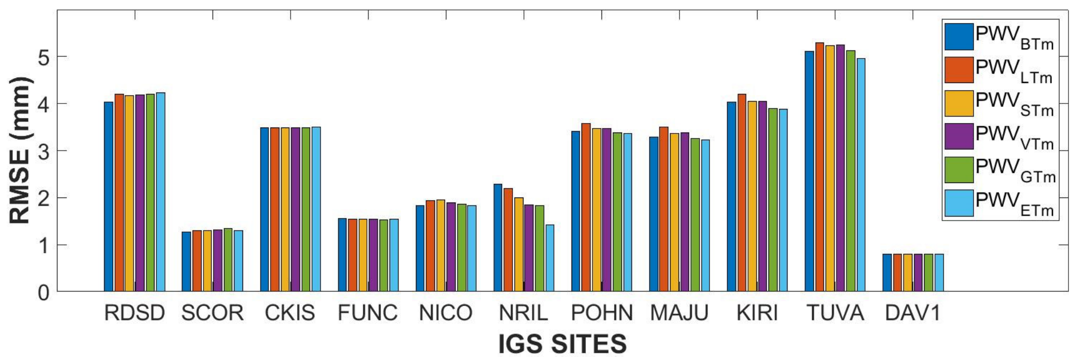

Figure 12: RMSE of PWV_{BTm}, PWV_{STm}, PWV_{VTm}, PWV_{GTm} and PWV_{ETm} compared with PWV_{RS} at 11 IGS stations in 2016. PWV unit is mm.

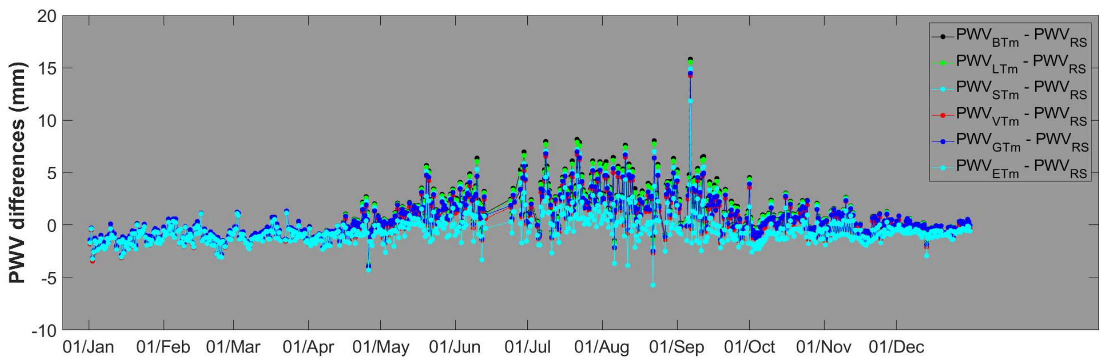

Figure 13: PWV differences of PWV_{BTm}, PWV_{LTm}, PWV_{STm}, PWV_{VTm} , PWV_{GTm} and PWV_{ETm} compared with PWV_{RS} at NIRL station in the year 2016. PWV unit is mm.

6. Summary and conclusion

In this study, we estimated T_m using the temperature and humidity profile data from the IGRA radiosonde data and the

ERA-Interim reanalysis datasets over the year 2009~2012. T_s was also extracted from the two data sets. Then, we analyzed the T_s-T_m relationship at each reanalysis grid node and radiosonde station. Analyses indicated that (1) The T_s-T_m relationship is stronger in the mid-high latitudes than in the low latitudes, (2) The T_s-T_m correlation coefficients are higher over the lands than over the oceans in the low latitudes, (3) the variation properties of T_s-T_m relationship are much more complicated rather than only dependence on the latitude, and (4) the T_s-T_m relationship has strong annual, semiannual, and diurnal variations in many areas.

Using the $0.75^\circ \times 0.75^\circ$ ERA-Interim datasets over the year 2009~2012, we developed two global gridded T_s-T_m models. The difference is that one model is static and another has time variations. The annual, semiannual, and diurnal variations in T_s-T_m relationship are considered in the time-varying model. Then, by comparing with the radiosonde data in 2016, we evaluated the T_m results from the different T_s-T_m models and the $1^\circ \times 1^\circ$ GPT2w model. Results demonstrate that our time-varying global gridded T_s-T_m model has a significant global precision advantage over the other global applied models. Average RMSE of T_m reduces by approximately 1 K. The proportion of the sites with small biases and RMSE increases significantly. At over 90 % of the radiosonde sites, the time-varying global gridded model has RMSE smaller than 4 K, while the RMSE more than 5 K nearly disappear. On the other hand, in the Bevis model or the latitude-related model, there are more than 17 % of the radiosonde sites having RMSE larger than 5 K. Multiple statistical tests at the 5 % significance level identified the significant superiority of the time-varying model at more than 60 % of the radiosonde sites. Analyses at the specific stations also demonstrate that the time-varying model can eliminate large errors in the estimated T_m series.

More precise T_s-T_m models also have positive impacts on the GPS-PWV retrievals. Regarding the GPS-PWV using ERA-Interim T_m estimates as the references, the relative errors of GPS-PWV using the time-varying global gridded T_s-T_m models are within 1.0 % at more than 74 % of our selected IGS sites. This result is clearly better than the other models. The differences between the GPS-PWV and the radiosonde PWV are approximately 1~5 mm. Some differences decrease 1~2 mm in the wetter conditions by using more precise T_m models. However, the error reductions of GPS-PWV due to the T_m models are very limited overall. This means that the other error sources, as we described in section 4.3, occupied the errors of GPS-PWV.

According to our experiments, we are confident that the time-varying global gridded T_s-T_m models presented here will help us to retrieve GPS PWV more precisely and to study the precise PWV variations in high temporal resolution as well as the T_s observations. Matlab array file consisting of the global gridded coefficients in our model, as well as codes to interpolate coefficients at any given location, are provided as the supplement of this study. It could be useful for researchers and applicants in relevant fields.

Data sets

Radiosonde data: ftp://ftp.ncdc.noaa.gov/pub/data/igra

ERA-Interim Project: https://doi.org/10.5065/D6CR5RD9

GPS-ZTD Product: ftp://cddis.gsfc.nasa.gov/pub/gps/products/troposphere/zpd

Our model Supplement: https://www.atmos-meas-tech-discuss.net/amt-2018-67/amt-2018-67-supplement.zip

Acknowledgments

This study is supported by National Natural Science Foundation of China (No. 41604028), the Anhui Provincial Natural Science Foundation (No. 1708085QD83), and the Doctoral Research Start-up Funds Projects of Anhui University (No. J01001966). The authors thank European Centre for Medium-Range Weather Forecasts for providing the ERA-Interim dataset. We also thank the National Centers for Environmental Information for the IGRA datasets and International GNSS Service for the GNSS troposphere products.

Competing interests

The authors declare that they have no conflict of interest.

References

Adams, D. K., Barbosa, H. M. J., and De Los Rios, K. P. G.: A Spatiotemporal Water Vapor-Deep Convection Correlation Metric Derived from the Amazon Dense GNSS Meteorological Network, Monthly Weather Review, 145, 279-288, 10.1175/mwr-d-16-0140.1, 2017.

Adler, B., Kalthoff, N., Kohler, M., Handwerker, J., Wieser, A., Corsmeier, U., Kottmeier, C., Lambert, D., and Bock, O.: The variability of water vapour and pre-convective conditions over the mountainous island of Corsica, Quarterly Journal Of the Royal Meteorological Society, 142, 335-346, 10.1002/qj.2545, 2016.

Bevis, M., Businger, S., Herring, T. A., Rocken, C., Anthes, R. A., and Ware, R. H.: GPS meteorology: Remote sensing of atmospheric water vapor using the global positioning system, Journal of Geophysical Research: Atmospheres, 97, 15787-15801, 10.1029/92JD01517, 1992.

Bohm, J., Moller, G., Schindelegger, M., Pain, G., and Weber, R.: Development of an improved empirical model for slant delays in the troposphere (GPT2w), Gps Solutions, 19, 433-441, 10.1007/s10291-014-0403-7, 2015.

Brown, M. B., and Forsythe, A. B.: Robust Tests for the Equality of Variances, Publications of the American Statistical Association, 69, 364-367, 1974.

Byun, S. H., and Bar-Sever, Y. E.: A new type of troposphere zenith path delay product of the international GNSS service, J. Geodesy, 83, 367-373, 10.1007/s00190-008-0288-8, 2009.

Campmany, E., Bech, J., Rodriguez-Marcos, J., Sola, Y., and Lorente, J.: A comparison of total precipitable water measurements from radiosonde and sunphotometers, Atmospheric Research, 97, 385-392, 10.1016/j.atmosres.2010.04.016, 2010.

Chen, P., Yao, W. Q., and Zhu, X. J.: Realization of global empirical model for mapping zenith wet delays onto precipitable water using NCEP re-analysis data, Geophys. J. Int., 198, 1748-1757, 10.1093/gji/ggu223, 2014.

Ciesielski, P. E., Chang, W. M., Huang, S. C., Johnson, R. H., Jou, B. J. D., Lee, W. C., Lin, P. H., Liu, C. H., and Wang, J. H.: Quality-Controlled Upper-Air Sounding Dataset for TiMREX/SoWMEX: Development and Corrections, Journal Of Atmospheric And Oceanic Technology, 27, 1802-1821, 10.1175/2010jtecha1481.1, 2010.

Haase, J., Ge, M., Vedel, H., and Calais, E.: Accuracy and variability of GPS tropospheric delay measurements of water vapor in the western Mediterranean, Journal of Applied Meteorology, 42, 1547-1568, 10.1175/1520-0450(2003)042<1547:AAVOGT>2.0.CO;2, 2003.

Hogg, R. V., and Ledolter, J.: Enginering Statistics, Macmillan, New York, 1987.

Itterly, K. F., Taylor, P. C., and Dodson, J. B.: Sensitivity of the Amazonian Convective Diurnal Cycle to Its Environment in Observations and Reanalysis, Journal of Geophysical Research: Atmospheres, 0, doi:10.1029/2018JD029251, 2018.

Jade, S., and Vijayan, M. S. M.: GPS-based atmospheric precipitable water vapor estimation using meteorological parameters interpolated from NCEP global reanalysis data, Journal of Geophysical Research-Atmospheres, 113, 10.1029/2007jd008758, 2008.

Jiang, P., Ye, S. R., Chen, D. Z., Liu, Y. Y., and Xia, P. F.: Retrieving Precipitable Water Vapor Data Using GPS Zenith Delays and Global Reanalysis Data in China, Remote Sensing, 8, 10.3390/rs8050389, 2016.

Karabatic, A., Weber, R., and Haiden, T.: Near real-time estimation of tropospheric water vapour content from ground based

GNSS data and its potential contribution to weather now-casting in Austria, Adv. Space Res., 47, 1691-1703, 10.1016/j.asr.2010.10.028, 2011.

Kealy, J., Foster, J., and Businger, S.: GPS meteorology: An investigation of ocean-based precipitable water estimates, Journal Of Geophysical Research-Atmospheres, 117, 10.1029/2011jd017422, 2012.

Lan, Z., Zhang, B., and Geng, Y.: Establishment and analysis of global gridded Tm − Ts relationship model, Geodesy and Geodynamics, 7, 101-107, https://doi.org/10.1016/j.geog.2016.02.001, 2016.

Lee, J., Park, J.-U., Cho, J., Baek, J., and Kim, H. W.: A characteristic analysis of fog using GPS-derived integrated water vapour, Meteorological Applications, 17, 463-473, 10.1002/met.182, 2010.

Li, X., Zhang, L., Cao, X. J., Quan, J. N., Wang, T. H., Liang, J. N., and Shi, J. S.: Retrieval of precipitable water vapor using MFRSR and comparison with other multisensors over the semi-arid area of northwest China, Atmospheric Research, 172, 83-94, 10.1016/j.atmosres.2015.12.015, 2016.

Liu, Z. Z., Li, M., Zhong, W. K., and Wong, M. S.: An approach to evaluate the absolute accuracy of WVR water vapor measurements inferred from multiple water vapor techniques, Journal Of Geodynamics, 72, 86-94, 10.1016/j.jog.2013.09.002, 2013.

Lu, C. X., Li, X. X., Nilsson, T., Ning, T., Heinkelmann, R., Ge, M. R., Glaser, S., and Schuh, H.: Real-time retrieval of precipitable water vapor from GPS and BeiDou observations, J. Geodesy, 89, 843-856, 10.1007/s00190-015-0818-0, 2015.

Mahoney, K., Jackson, D. L., Neiman, P., Hughes, M., Darby, L., Wick, G., White, A., Sukovich, E., and Cifelli, R.: Understanding the role of atmospheric rivers in heavy precipitation in the Southeast US, Monthly Weather Review, 10.1175/MWR-D-15-0279.1, 2016.

Means, J. D.: GPS Precipitable Water as a Diagnostic of the North American Monsoon in California and Nevada, J. Clim., 26, 1432-1444, 10.1175/jcli-d-12-00185.1, 2013.

Means, J. D., and Cayan, D.: Precipitable Water from GPS Zenith Delays Using North American Regional Reanalysis Meteorology, Journal of Atmospheric and Oceanic Technology, 30, 485-495, 10.1175/jtech-d-12-00064.1, 2013.

Ning, T., Elgered, G., Willen, U., and Johansson, J. M.: Evaluation of the atmospheric water vapor content in a regional climate model using ground-based GPS measurements, Journal Of Geophysical Research-Atmospheres, 118, 329-339, 10.1029/2012jd018053, 2013.

Ning, T., Wang, J., Elgered, G., Dick, G., Wickert, J., Bradke, M., Sommer, M., Querel, R., and Smale, D.: The uncertainty of the atmospheric integrated water vapour estimated from GNSS observations, Atmos. Meas. Tech., 9, 79-92, 10.5194/amt-9-79-2016, 2016.

Pacione, R., and Vespe, F.: Comparative studies for the assessment of the quality of near-real-time GPS-derived atmospheric parameters, Journal of Atmospheric and Oceanic Technology, 25, 701-714, 10.1175/2007jtecha935.1, 2008.

Perez-Ramirez, D., Whiteman, D. N., Smirnov, A., Lyamani, H., Holben, B. N., Pinker, R., Andrade, M., and Alados-Arboledas, L.: Evaluation of AERONET precipitable water vapor versus microwave radiometry, GPS, and radiosondes at ARM sites, Journal Of Geophysical Research-Atmospheres, 119, 9596-9613, 10.1002/2014jd021730, 2014.

Raju, C. S., Saha, K., Thampi, B. V., and Parameswaran, K.: Empirical model for mean temperature for Indian zone and estimation of precipitable water vapor from ground based GPS measurements, Ann. Geophys., 25, 1935-1948, 2007.

Rocken, C., Johnson, J., Van Hove, T., and Iwabuchi, T.: Atmospheric water vapor and geoid measurements in the open ocean with GPS, Geophysical Research Letters, 32, 10.1029/2005gl022573, 2005.

Rohm, W., Yuan, Y. B., Biadeglgne, B., Zhang, K. F., and Le Marshall, J.: Ground-based GNSS ZTD/IWV estimation system for numerical weather prediction in challenging weather conditions, Atmospheric Research, 138, 414-426, 10.1016/j.atmosres.2013.11.026, 2014.

Sheng, P., Mao, J., Li, J., Ge, Z., Zhang, A., Sang, J., Pan, N., and Zhang, H.: Atmospheric Physics 2ed., Peking University Press, Beijing, 2013.

Singh, D., Ghosh, J. K., and Kashyap, D.: Weighted mean temperature model for extra tropical region of India, Journal of Atmospheric and Solar-Terrestrial Physics, 107, 48-53, http://dx.doi.org/10.1016/j.jastp.2013.10.016, 2014.

Snajdrova, K., Boehm, J., Willis, P., Haas, R., and Schuh, H.: Multi-technique comparison of tropospheric zenith delays derived during the CONT02 campaign, J. Geodesy, 79, 613-623, 10.1007/s00190-005-0010-z, 2006.

Song, J. J., Wang, Y., and Tang, J. P.: A Hiatus of the Greenhouse Effect, Sci Rep, 6, 9, 10.1038/srep33315, 2016.

Van Baelen, J., and Penide, G.: Study of water vapor vertical variability and possible cloud formation with a small network of GPS stations, Geophysical Research Letters, 36, 10.1029/2008gl036148, 2009.

Wang, J. H., Zhang, L. Y., and Dai, A.: Global estimates of water-vapor-weighted mean temperature of the atmosphere for GPS applications, Journal of Geophysical Research-Atmospheres, 110, 10.1029/2005jd006215, 2005.

Wang, X. M., Zhang, K. F., Wu, S. Q., Fan, S. J., and Cheng, Y. Y.: Water vapor-weighted mean temperature and its impact on the determination of precipitable water vapor and its linear trend, Journal Of Geophysical Research-Atmospheres, 121, 833-852, 10.1002/2015jd024181, 2016.

Wang, X. Y., Song, L. C., and Cao, Y. C.: Analysis of the weighted mean temperature of china based on sounding and ECMWF reanalysis data, Acta Meteorol. Sin., 26, 642-652, 10.1007/s13351-012-0508-2, 2012.

Yao, Y., Zhang, B., Xu, C., and Yan, F.: Improved one/multi-parameter models that consider seasonal and geographic variations for estimating weighted mean temperature in ground-based GPS meteorology, J. Geodesy, 88, 273-282, 10.1007/s00190-013-0684-6, 2014a.

Yao, Y. B., Zhu, S., and Yue, S. Q.: A globally applicable, season-specific model for estimating the weighted mean temperature of the atmosphere, J. Geodesy, 86, 1125-1135, 10.1007/s00190-012-0568-1, 2012.

Yao, Y. B., Zhang, B., Xu, C. Q., and Chen, J. J.: Analysis of the global T(m)-T(s) correlation and establishment of the latitude-related linear model, Chinese Science Bulletin, 59, 2340-2347, 10.1007/s11434-014-0275-9, 2014b.